LAWRENCE
LIVERMORE
NATIONAL
LABORATORY

LLNL-JRNL-420715

Strong stabilization of the Rayleigh-Taylor instability by material strength at Mbar pressures

H.-S. Park, K. T. Lorenz, R. M. Cavallo, S. M. Pollaine, S. T. Prisbrey, R. E. Rudd, R. C. Becker, J. V. Bernier, B. A. Remington

November 24, 2009

Physics of Plasmas

Disclaimer

Strong stabilization of the Rayleigh-Taylor instability by material strength at Mbar pressures

Hye-Sook Park, K. T. Lorenz, R. M. Cavallo, S. M. Pollaine, S. T. Prisbrey,
R. E. Rudd, R. C. Becker, J. V. Bernier, and B. A. Remington

Lawrence Livermore National Laboratory, Livermore, CA 94550 USA

Experimental results showing significant reductions from classical in the Rayleigh-Taylor (RT) instability growth rate due to high pressure effective lattice viscosity are presented. Using a laser created ramped drive, vanadium samples are compressed and accelerated quasi-isentropically at ~1 Mbar pressures, while maintaining the sample in the solid-state. Comparisons with simulations and theory indicate that the high pressure, high strain rate conditions trigger a phonon drag mechanism, resulting in the observed high effective lattice viscosity and strong stabilization of the RT instability,

PACS numbers: 62.50.-p, 62.20.-x, 62.20.F, 68.35.Gy

When a low density fluid of density ρ_L accelerates a higher density fluid of density ρ_H, conditions for the buoyancy driven Rayleigh-Taylor (RT) instability are set up [1,2]. Perturbations at the interface can grow, generating "bubbles" of the lower density fluid rising into the denser fluid, and "spikes" of the latter sinking through the low density fluid [3]. The RT instability is important to many fields of science, such as initial confinement fusion (ICF) [4-7], supernova explosions [8,9], asteroid impact dynamics [10], and Earth interior dynamics and plate tectonics [11]. The RT instability growth depends on the Atwood number $A = (\rho_H - \rho_L)/(\rho_H + \rho_L)$, the acceleration g, and the perturbation wave number $k = 2\pi/\lambda$, where λ is the perturbation wavelength. Suppression mechanisms have been reported due to self radiation [12], thermal diffusion [13-15], convection [16a], "snowplow" mechanism [16b],

and ablation [17-21].We present experimental and simulation results that demonstrate another RT instability stabilization mechanism at high pressure, namely, effective lattice viscosity by phonon drag. This high pressure stabilization mechanism is predicted to increase with pressure, provided the solid-state lattice is maintained.

We illustrate the basic material deformation mechanisms schematically in Fig. 1a. [Meyers 1994; Regazzoni, 1987] The fundamental carriers of deformation in a solid-state sample are dislocations. The resistance to dislocation transport is the microscopic basis for material strength. Although one by one, dislocations move in step sizes of order the crystal lattice spacing, in step sizes called a Burgers vector, b. When large numbers of dislocations, of order $\sim 10^4$, move in concert, macroscopic deformation occurs. Generally dislocations in solid pre-exist, and are pinned against barriers, as shown in the inset of Fig. 1a. When a shear stress is applied, in our experiments, generated by the RT instability, they may remain pinned, depending on the height and extent of the barrier. In this case, thermal fluctuations in the lattice can kick the dislocation over the barrier, after which it will glide along a glide plane till it gets pinned (stopped) at another barrier. This mechanism of deformation is called thermal activation. If the applied shear stress is sufficiently strong, however, the dislocations can be pushed over the tops of all barriers, also illustrated in the inset of Fig. 1a. In this case, the resistance to the dislocation motion can come from scattering of lattice phonons, and this regime of deformation is referred to as phonon drag. If dislocation velocity is plotted versus applied shear stress, these two regimes of deformation are illustrated in Fig. 1a. In the thermal activation regime, the dislocation velocity increases exponentially with an increasing shear stress, whereas in the illustration in Fig. 1a, the increase of velocity with shear stress in the phonon drag regime is linear.

The starting point in constructing a strength model is Orowan's equation, [Meyers, 1994]

$$d\varepsilon/dt = \rho_{disloc}.b.\langle v_{disloc}\rangle \quad , \qquad \text{(Eq. 1)}$$

where ε is plastic strain (such as a change in rippled amplitude, Δη, due to the RT instability, normalized by the rippled wavelength, $\varepsilon \sim \Delta\eta/\lambda$), $d\varepsilon/dt$ is strain rate, ρ_{disloc} is mobile dislocation density, b is the Burgers vector, and $< v_{disloc} >$ is the average dislocation velocity. One then writes down relationships for average dislocation velocity in the thermal activation regime and phonon drag regime, and inserts these into Eq. 1. [Regazzoni, 1987] Two popular models that result are the Steinberg-Lund model, [Steinberg, 1989 (ref. 32)] and the Preston-Tonks-Wallace or PTW model [Preston, 2003 (ref. 30)]. The results of these two models, for their default parameters for vanadium are shown in Fig. 1b. The conditions assumed in Fig. 1b are pressure, temperature, and compression of 0.5 Mbar, 700 K, and 30%. One sees that these two models of material strength differ significantly on the critical strain rate at which the deformation transitions from thermal activation to phonon drag. Once in the phonon drag regime, the Steinberg-Lund model assume strength, σ, varies linearly with strain rate, $\sigma \sim d\varepsilon/dt$, whereas PTW assumes strength increases as $(\sigma \sim d\varepsilon/dt)^{1/4}$. The modified PTW curve in Fig. 1b will be discussed further later in this paper. [Remington, 2006 (ref. 31); Remington, MMTA 2004]

A typical target in our experiment has a "reservoir" consisting of 40 μm thick polyimide, 125 μm thick polycarbonate, and 35 μm thick brominated polystyrene, $C_{50}H_{48}Br_2$, glued together. This is followed by a 300 μm vacuum gap, then the rippled V sample, made by sputtering V onto a mandrel that has sinusoidal ripples of 60 μm wavelength and 0.6 μm amplitude machined onto its surface. The back surface of the V is polished flat, then the mandrel is chemically removed. The vanadium samples were full density, had an average grain size of ~ 1 μm in the lateral direction, 3-5 μm in the thickness (columnar) direction, and a measured tensile strength at ambient pressure and low strain rate of 7.15 kbar [22]. To thermally insulate the rippled V sample from the heat created by the stagnating plasma, we use a 6 μm thick, CH-based epoxy "heat shield", conformal on the ripple side and machined flat on

the gap side. The drive calibration shots replaced the rippled V package with 10 μm Al backed by a 500 μm LiF window for interface velocity measurements.

We use six azimuthally symmetric laser beams at the Omega Laser, University of Rochester, each with E_L~135 J energy at laser wavelength of λ_L=351 nm and 3.7 ns square pulse shape, to generate our drive. The ~640 μm diameter flat-top spatial profile is achieved using continuous phase plates (CPP) on the drive beams [23], creating an average peak laser intensity of $I_L \sim 2.5 \times 10^{13}$ W/cm^2. This launches a strong shock through the reservoir which, at shock breakout, releases as a plasma across the 300 μm vacuum gap and stagnates on the V sample, creating a ~1 Mbar ramped pressure drive, as illustrated schematically in Fig.2a [24,25]. Based on Newton's second law, $P \sim \rho g \Delta z$, this causes the Δz =35 μm thick V sample to accelerate at a peak value of $g \sim 5 \times 10^{13}$ cm/s^2 (0.5 μm/ns^2). The accelerating sample is RT unstable; the ripple amplitude increases at a rate that is reduced due to material strength. Density plots from 2D simulations at a sequence of times, shown in Fig. 2b, illustrate the stabilization of RT growth due to material strength. The particle velocity (u_p) of the Al-LiF interface was measured by a line VISAR (velocity interferometer system for any reflector) diagnostic [26 and references therein] for a range of laser energies, as shown in Fig. 3d. VISAR is an interferometer with unequal path delays that measures the motion of the reflecting surface. From simulations with the radiation-hydrodynamics code LASNEX [27] adjusted to reproduce this VISAR data, we generate the plasma drive: a set of material density, velocity, and temperature profiles as a function of position from the unloading reservoir just prior to impacting the sample, as illustrated in the lower inset of Fig. 3a-c. This plasma drive applied to the V sample generates a ramped loading reaching P_{max}~900 kbar, as shown in Fig. 3e, at peak compressions of $\rho/\rho_0 \sim 1.3$-1.4. The sample is predicted to stay factors of 3-5 below the calculated melt temperature based on the Lindemann law [28], as shown in the inset in Fig. 3f.

To measure the RT ripple growth, we used face-on radiography with a 5.2 keV laser driven vanadium He-α x-ray backlighter. For area backlighting, we use a large area x-ray source and a gated x-ray camera with a 2 x 2 array of 15 μm pinholes configured at magnification of ~6 [29]. Alternatively, we use a ~15 μm diameter pinhole aperture placed just in front of the V backlighter foil to create a point source for projection imaging at magnification of ~19, onto a gated x-ray camera. Figure 4a shows example radiographs recorded at 40 - 130 ns. The contrast (light and dark bands or strips) are due to variations in transmitted backlighter x-ray intensity, $I = I_0 \exp(-z / \lambda_{mfp})$, where λ_{mfp} is the x-ray mean free path length, and z is the vanadium foil thickness. The RT growth causes foil thickness modulations of increasing depth, Δz, which cause x-ray optical depth modulations, $\Delta OD = \Delta z/\lambda_{mfp}$. The left side of Fig. 4b shows lineouts of radiographic images of the ripples averaged over a 120 μm vertical window at delay times of 40 ns and 80 ns relative to the start of the drive laser, compared with fits using $\ln(I_v/I) = a \cdot \sin(\frac{2\pi}{\lambda} - \varphi)$. Here I is the average intensity through the rippled foil, I_v is the intensity in the ripple valleys (brighter regions), and a, λ and φ are the fitted amplitude, wavelength and the phase of the ripple. The perturbation growth is written as a growth factor, $GF(t) = \Delta OD(t)/(\Delta OD_0 \cdot MTF)$, where $\Delta OD(t)$ is the modulation in optical depth at time *t* due to the ripple, $\Delta OD_0 = \eta_0/\lambda_{mfp}$ is the initial optical depth, where λ_{mfp}~19.6 μm is the mean free path length of the 5.2 keV backlighter x rays in vanadium, and is quantified by step-wedge measurements, as shown in Figs. 5a and 5b. The MTF is the modulation transfer function, which quantifies the effect of the instrument spatial resolution on the ripple contrast measurements. The $\Delta OD(t)$ is determined from the radiograph by a Fourier analysis of the ripple lineouts. The MTF, which quantifies the diagnostic spatial resolution, is measured on separate shots using a resolution grid, as shown in Figs. 5c and 5d: MTF > 0.8 for the λ = 60 μm ripples used in this experiment.

We compare our RT growth factor measurements to the results from 2D radiation-hydrodynamics simulations including a constitutive strength model. The Preston-Tonks-Wallace (PTW) strength model is strain rate dependent, and is based on the deformation mechanisms of thermal activation for low strain rates (which assumes dislocations are pinned against stress barriers in the lattice and require a thermal "kick" to surmount the barrier and glide to the next pinning site) and viscous phonon drag for high strain rates (which assumes dislocations are gliding over the tops of stress barriers, resisted only by the drag from scattering of lattice phonons) [30]. The PTW strength in the low-strain limit is expressed as:

$$\sigma_y = 2G \max\left\{ y_0 - (y_0 - y_\infty)\mathrm{erf}[k\hat{T}\ln(\gamma\dot{\xi}/\dot{\varepsilon})],\ s_0(\dot{\varepsilon}/\gamma\dot{\xi})^{\beta} \right\}, \qquad \text{(Eq. 2)}$$

where $G = G(P,T)$ is the pressure dependent shear modulus, erf is the mathematical error function, $\dot{\varepsilon}$ is the strain rate, $\hat{T} = T / T_{melt}$ is the normalized temperature, $T_{melt}(\rho)$ is the Lindeman law melt temperature [28], $\dot{\xi}$ is a reference inverse time scale, $\gamma\dot{\xi} = \dot{\varepsilon}_{crit}$ is the critical strain rate above which the deformation switches from thermal activation to phonon drag, and y_0, y_∞, κ, γ, s_0, and β are material dependent input parameters. These parameters roughly correspond material properties according to $\gamma \sim \rho_{disloc} b^2$, $\kappa \sim 1/U_k$, $y_\infty \sim \sigma_A$, $y_0 \sim \sigma_A + \sigma_P$, and $y_0 - y_\infty \sim \sigma_P$, where ρ_{disloc}, b, U_k, σ_A, and σ_P represent dislocation density, Burgers vector, kink activation energy, athermal strength component, and Peierls stress, respectively. [29b] The PTW strength, σ_s, in the high-strain (saturated) limit has a similar form, only with s_0 and s_∞ replacing y_0 and y_∞. These are combined in a Voce work hardening prescription for arbitrary strain, ε [30]. We will also show comparisons to an older model, the Steinberg-Guinan model, [Steinberg, 1980], which is written as,

$$\sigma = \sigma_0 f(\varepsilon)\left[1 + \left(\frac{G_P'}{G_0}\right)\frac{P}{\eta^{1/3}} + \left(\frac{G_T'}{G_0}\right)(T - 300)\right], \qquad \text{(3a)}$$

$$G = G_0\left[1+\left(\frac{G_P'}{G_0}\right)\frac{P}{\eta^{1/3}}+\left(\frac{G_T'}{G_0}\right)(T-300)\right], \tag{3b}$$

$$f(\varepsilon) = [1+\beta(\varepsilon_i+\varepsilon)]^n \tag{3c}$$

This model is largely a first order Taylor expansion in pressure and temperature, with a work hardening prefactor which is a power law in strain, ε. And we discuss briefly the Steinberg-Lund model, which is written as

$$\sigma = [\sigma_T(\dot{\varepsilon},T)+\sigma_A f(\varepsilon)]\frac{G(P,T)}{G_0} \tag{4a}$$

$$\dot{\varepsilon} = \frac{1}{\frac{1}{C_1}\exp\left[\frac{2U_k}{kT}\left(1-\frac{\sigma_T}{\sigma_P}\right)^2\right]+\frac{C_2}{\sigma_T}} \tag{4b}$$

Note, the Steinberg-Guinan model is independent of strain rate. The Steinberg-Lund model is strain-rate dependent, and in the phonon drag regime, gives a linear dependence of strength on strain rate. The PTW is also strain rate dependent, but in the phonon drag regime, strength increases roughly as strain rate to the ¼ power.

After normalizing to the laser energy of 820 J, the self-consistent data set of *GF(t)* spanning several shot campaigns is shown by the red square symbols in Fig. 6a. Typical experimental errors are estimated to be *δGF/GF* ~10% or less. We estimate an average strain rate, $\dot{\varepsilon}_{av}$ ~3 x 10^7 s^{-1}, by fitting a linear slope to the calculated strain over the interval of 25-40 ns. For t > 40 ns, this drops to $\dot{\varepsilon}_{av}$ ~ 3 x 10^6 s^{-1}. The top curve corresponds to a 2D simulation of the RT growth assuming no strength, and overpredicts the experimental data at 70 ns by a factor of ~6. Simulations using the PTW model with the default input parameters [30] is the next highest curve; which also considerably over-predicts the

experimental data. To fit our experimental data with the PTW model in Fig. 6a, we lowered the critical strain rate for the transition from the thermal activation to the phonon drag regime from the default value of $\gamma\dot{\xi} \sim 10^9$ s^{-1} to $\sim 10^6$ s^{-1}, accomplished by multiplying the PTW input parameters γ, y_0, and s_0 by 1/800, 0.60, and 0.68, respectively [31]. The default PTW parameters for V in the high-$\dot{\varepsilon}$ regime were set by overdriven shock experiments in Ta, also a BCC metal [30]. Furthermore, the strain rate interval of 10^4-10^9 s^{-1} was not modeled but rather "filled in" with PTW, due to the absence of reliable data to fit. So, it is not surprising that substantial changes in these input parameters for ramp loaded V were required. These changes to the PTW input parameters leave the strength predictions at $\dot{\varepsilon} < 10^6$ s^{-1} (thermal activation regime) largely unchanged, while increasing the strength for $\dot{\varepsilon} > 10^6$ s^{-1} (phonon drag regime), as shown in Fig. 1b (the curve labeled "modified PTW"). It is interesting to note that the Steinberg-Lund strength model [32], also shown in Fig. 1b, which has several features similar to the PTW model, predicts the transition from thermal activation to phonon drag in vanadium would occur at $\dot{\varepsilon}_{crit} \sim 10^5$ s^{-1} for default input parameters. Hence, the critical strain rate for the transition from thermal activation to phonon drag is uncertain by factors of 10^3-10^4, due to the lack of data in this ultrahigh-$\dot{\varepsilon}$ regime. The dotted red curve in Fig. 3e shows the spatially averaged V strength vs. time for the PTW model, after averaging over ~nsec level temporal fluctuations; the maximum strength occurs at the time of peak pressure and strain rate. The calculated peak strength for our RT experiments, $\sigma_{max} \sim 24$ kbar, corresponds to a peak pressure and strain rate of 900 kbar and 3 x 10^7 s^{-1}. This is a factor of 3.5 higher than the measured ambient strength of 7.15 kbar [22]. Recent theoretical work shows that the shear modulus is not expected to increase significantly with pressure in this pressure range [33]. This suggests that our observed strength increase is due to rate effects rather than pressure. We estimate an overall ~20% uncertainty in our $\sigma_{max} \sim 24$ kbar peak strength result, based on 10% due to the uncertainties in the growth factor measurements, 10% due to the uncertainties in our plasma drive, and 10% due to any

potential model dependence in our analysis, all added in quadrature. During this extended series of V-RT shots, we also did shots where the peak pressure varied from 770 kbar to 950 kbar. For each shot, we inferred a peak strength by the methods describe above, and these are plotted in the inset of Fig. 6a. Both models give peak strength increasing with peak pressure, but more importantly, both models give the same peak strength. So independent of which strength model we use, once the settings in the model have been adjusted to reproduce the RT experiment, they give the same predicted peak strength (corresponding to peak pressure). This suggests our experiments are more than just a test of strength models at high pressures and strain rates, but a means of inferring peak strength itself, albeit indirectly.

We now compare to an analytic RT growth model that treats strength as an effective lattice viscosity. In the linear regime, classical RT growth can be written as $GF \approx e^{\int \gamma_{classical} dt}$, where $\gamma_{classical} \approx [A \cdot \frac{2\pi}{\lambda} \cdot g(t)]^{1/2}$ gives the growth rate for inviscid fluids, and A, λ, and g are the Atwood number, perturbation wavelength, and foil acceleration, respectively. For viscous fluids, the RT growth rate is determined from $\gamma_{RT}^2 + 2k^2 \nu \gamma_{RT} - gkA = 0$ [34, 35], where $\nu(cm^2/s) = \mu/\rho$ is the kinematic viscosity, μ(dyne·sec/cm^2=poise) is the dynamic viscosity, and ρ is density. We show these analytic results for RT growth factors versus perturbation wavelength at 70 ns in Fig. 6b. Experimental data were taken at λ = 40 and 60 μm (red squares). The 2D simulations were done at λ = 40, 60, and 100 μm with the modified strength models (blue diamonds, green triangles), and with strength turned off (black circles). The smooth curves in Fig. 5 correspond to (in order from the top) dynamic viscosities of 0, 100, 200, 400, and 800 poise, with a best fit at ~400 poise We show also in Fig. 6a the growth factor time evolution for the viscous model using 400 poise. As a consistency check, we use a relationship equating strength with an effective lattice viscosity, $\nu = \mu / \rho \approx \sigma / (\sqrt{6} \rho \langle \dot{\varepsilon} \rangle)$ [35], giving $\sigma \approx \sqrt{6} \langle \dot{\varepsilon} \rangle \mu$. Using an average strain rate of $\langle \dot{\varepsilon} \rangle \approx 3 \times 10^7$ s^{-1} over the interval of 25-40 ns from the 1D radiation-

hydrodynamics simulations and the fitted viscosity of 400 poise gives an estimated peak strength of σ_{max}~29 kbar. For a second estimate, we make a rough approximation of strain rate from $\langle \dot{\varepsilon} \rangle \approx \frac{1}{3} \dot{\rho} / \rho \approx \frac{1}{3} (\Delta\rho / \rho_0) / \Delta t_{rise.time}$ [24]. The equation of state of V [36], allows an estimate of compression at $\rho/\rho_0 \sim 1.4$, which occurs over the measured rise time of ~6 ns, giving $\langle \dot{\varepsilon} \rangle \approx 2 \times 10^7$ s^{-1}. This gives a second estimate of peak strength of σ_{max}~19 kbar. These two analytic approximations bracket to within ~20% the more accurate result for the strength at peak pressure of σ_{max}~24 kbar inferred from the 2D RT simulations, shown in Fig. 2b.

We now connect our inferred macroscopic fluid viscosity of ~400 poise to the microscopic dislocation drag coefficient in the phonon drag regime of high strain rate deformation. A macroscopic viscosity for our experiment can be defined as $\sigma_{shear} \sim \mu \cdot v_{RT}/\lambda_{RT}$, where μ is the dynamic viscosity, σ_{shear} is the shear stress leading to the RT growth, v_{RT} is the RT bubble velocity for perturbation of wavelength λ_{RT}. At the lattice level, applied shear stress is related to dislocation terminal velocity by $M \cdot \sigma_{shear} \cdot b = B \cdot v_{disloc}$, where M~3 is the Taylor factor (to account for the glide plane orientation), b is the Burger's vector, and B is the dislocation drag coefficient. [37] And finally, Orowan's equation relates macroscopic strain rate to microscopic parameters, $d\varepsilon/dt = \rho_{disloc} \cdot b \cdot v_{disloc}$, where ρ_{disloc} is the dislocation density. These three equations can be combined to give $\mu/B \approx (v_{disloc}/v_{RT}).(\lambda_{RT}/b)/M \sim 1/(M \cdot \rho_{disloc} \cdot b^2)$. Taking a dislocation density of ~10^{11} cm^{-2} from a multi-scale simulation of our RT experiment (see Fig. 7) at peak pressure, [38], and assuming b ~ 2.5 Angstroms under compression, gives $\mu/B \sim 5 \times 10^3$. We conclude that our inferred effective lattice viscosity of ~400 poise corresponds to a dislocation drag coefficient of ~0.08 dyne·s/cm^2 in the phonon drag regime under the peak pressure (~1 Mbar) and high strain rate (~10^7 s^{-1}) conditions of our vanadium RT experiment.

Acknowledgement: This work was performed under the auspices of the U.S. Department of Energy by Lawrence Livermore National Laboratory under Contract DE-AC52-07NA27344.

References:

[Becker, 2009] R. Becker, A. Arsenlis, J. Marian, M. Rhee, M. Tang, and L. Yang, "Continuum level formulation and implementation of a multi-scale model for vanadium," LLNL Internal Report No. LLNL-TR-416095 (August, 2009).

[Remington, 2004] B.A. Remington et al., Met. Mat. Trans. 35A, 2587 (2004).

[Meyers, 1998] M.A. Meyers textbook (1994).

[1] Lord Rayleigh, Phil. Mag. 34, 145 (1892).

[2] G. Taylor, Proc. R. Soc. A 201, 192 (1950).

[3] D. H. Sharp, Physica D 12, 3 (1984).

[4] J. Nuckolls, L. Wood, A. Thiessen, and G. Zimmerman, Nature 239, 139 (1972).

[5] A. J. Cole, J. D. Kilkenny, P.T. Rumsby, *et al*., Nature 299, 329 (1982).

[6] R.L. McCrory, L. Montierth, R.L. Morse, and C. P. Verdon, Phys. Rev. Lett. 46, 336 (1981).

[7] J. D. Lindl and W. C. Mead, Phys. Rev. Lett. 34, 1273 (1975).

[8] E. Muller et al., Astron. Astrophys. 251, 505 (1991).

[9] K. Kifonidis et al., Astron. Astrophys. 453, 661 (2006).

[10] M.-M. MacLow and K. Zahnle, Astrophys. J. Lett. 434, L33 (1994); V.V. Shuvalov *et al*., Planetary and Space Science 50, 181 (2002).

[11] B. J. P. Kaus and Y. Y. Podladchikov, Geophys. Res. Lett. 28, 11095 (2001); P. Molner, G.A. Houseman, and C.P. Conrad, Geophys. J. Int. 133, 568 (1998); G. A. Houseman, P. Molnar, Geoph. J. Int.,128, 125 (1997); Yu. Yu. Podladchikov, C. Talbot, A. N. B. Poliakov, Tectonophysics, 228, 349 (1993).

[12] S. Fujioka, A. Sunahara, K. Nishihar, *et al*., Phys. Rev. Lett. 92, 195001 (2004).

[13] L. Masse, Phys. Rev. Lett. 98, 245001 (2007);

[14] A. Sunahara, J. A. Delettrez, C. Stoeckl, *et al*., Phys. Rev. Lett. 91, 095003 (2003);

[15] E. Ott and D.A, Russell, Phys. Rev. Lett. 41, 1048 (1978).

[16a] A.B. Budko and M.A. Liberman, Phys. Rev. Lett. 68, 178 (1992).

[16b] S.M. Gol'Berg and A.L. Velikovich, "Supression of Tayleigh-Taylor instability by the snowplow mechanism," Phys. Fluids B 5, 1164 (1990).

[17] V. A. Smalyuk, S. X. Hu, V. N. Goncharov, *et al*., Phys. Rev. Lett. 101, 025002 (2008).

[18] V. Lobatchev, R. Betti, Phys. Rev. Lett. 85, 4522 (2000).

[19] J. D. Lindl, Phys. Plasmas 2, 3933 (1995).

[20] R. Betti et al., Phys. Plasmas 2, 3844 (1995).

[21] H. Takabe et al., Phys. Fluids 28, 3676 (1985).

[22] A.F. Jankowski, J. Go, and J.P. Hayes, Surface & Coatings Tech. 202, 957 (2007).

[23] C.A. Haynam *et al*., Appl. Optics 46, 3276 (2007).

[24] J. Edwards *et al*., Phys. Rev. Lett. 92, 075002 (2004).

[25] K.T. Lorenz *et al*. HEDP 2, 113 (2006).

[26] R. Barker and J.. Hollenbach. Appl. Phys. 43, 4669 (1972); P. M. Celliers et al, Rev. Sci. Instrum. 75, 4916 (2004); P. M. Celliers *et al*., Appl. Phys. Lett. 73, 1320 (1998).

[27] G. B. Zimmerman and W.L. Kruer, Com. Plasma Phys. Control. Fusion 2, 51 (1975).

[29] K. T. Lorenz *et al*. Phys. Plasmas 12, 056309 (2005).

[29b] B.A. Remington et al., in Shock Compression of Condensed Matter – 2005, edited by M.D. Furnish, M. Elert, T.P. Russell, and C.T. White (AIP, 2006), p. 765.

[30] D. L. Preston, D. L. Tonks, and D. C. Wallace, J. Appl. Phys. 93, 211 (2003).

[31] B. A. Remington et al., Mat. Sci. Tech. 22, 474 (2006); ibid, submitted, HEDP (2009).

[32] D. J. Steinberg and C. M. Lund, J. Appl. Phys. 65, 1528 (1989).

[33] R. E. Rudd and J. E. Klepeis, J. Appl. Phys. 104, 093528 (2008).

[34] K. O. Mikaelian, Phys. Rev. E 47, 375 (1993).

[35] J. D. Colvin et al., J.Appl.Phys. 93, 5287 (2003).

[36] *High-Velocity Impact Phenomena*, Ed. Ray Kinslow (Academic Press, New York, 1970), pg. 538.

[37] Marc Andre Meyers and Krishan Kumar Chawla, Mechanical Metallurgy: Principles and Applications (Prentice-Hall, 1984).

[38] R. Becker et al., "Continuum level formulation and implementation of a multiscale model for vanadium, LLNL internal report, LLNL-TR-416095 (August, 2009).

Fig. 1. (a) Sketch of dislocation velocity versus applied shear stress. The inset shows schematically an edge dislocation pinned against a barrier in stress vs. position. [Adapted from Meyers, 1994] (b) Preston-Tonks-Wallace (PTW) strength model vs. log($\dot{\varepsilon}$) for the low strain limit (σ_y) and the saturated, high strain limit (σ_s) for default (solid) and for the modified (dashed) input parameters, assuming pressure P = 500 kbar, temperature T = 500 K, and compression $\rho/\rho_0 = 1.236$ in vanadium. [Preston, 2003] Also shown is the Steinberg-Lund model [Steinberg, 1989]. The curved labeled "Modified PTW" has lowered the critical strain rate in the model at which the strength transitions from thermal activation to phonon drag, while keeping the lower strain regime largely unchanged.

Fig. 2. (a) Schematic illustrating the experimental configuration. Drive lasers shock a plastic reservoir, which releases across a vacuum gap as a flowing plasma atmosphere. This generates a ramped pressure drive, upon stagnation on the vanadium (V) sample. A second set of lasers, delayed in time, drives an x-ray backlighter for face-on radiography of the Rayleigh-Taylor (RT) instability growth in the rippled V sample. The drive (applied pressure vs. time) is measured on similar targets only replacing the rippled vanadium with 10 μm of Al backed by a 500 μm LiF window for VISAR measurements. On the far right side, a raw experimental VISAR velocity image (top), and a 2D face-on radiograph of a rippled V RT sample at 80 ns (bottom) are shown. (b) Density plots of the RT growth from 2D radiation-hydrodynamics simulations at 45, 55, 65, and 75 ns, using the PTW strength model with input parameters modified to reproduce the RT data shown in Fig. 4. The second plot at 75 ns (far right hand side) is for a simulation where V has no strength, showing the much greater RT growth.

Fig. 3. Plasma drive calculation and characterization measurements to infer applied pressure vs. time in the vanadium sample. (a) The result of the "plasma drive: velocity vs. position just prior to the releasing plasma impacting the Al-LiF drive package. (b) Same as (a) only density vs. position. (c) Same as (a) only temperature vs position. (d) Line VISAR measurements of particle velocity at the Al-LiF interface for a 10 μm Al foil backed by a ~500 μm thick LiF window at four different laser energies, E_L =743, 776, 790, and 818 J. The inset shows the result of a simulation giving density vs. position, $\rho(z)$, of the shock-released reservoir "plasma drive" just before stagnating on the vanadium sample, adjusted to reproduce the Al-LiF drive shots. (e) Corresponding pressure vs. time in the vanadium sample (solid black curve), as calculated from the radiation-hydrodynamics simulations. The dotted red curve gives the strength vs. time predicted from the simulation using the PTW strength model with input parameters

modified to reproduce the RT experiment, shown in Fig. 4. (f) The Lindemann Law melt temperature (red curve) and sample temperature (blue curve) from the simulations.

Fig. 4. Results from the in-flight x-ray radiographs of the driven V-RT samples. (a) Example x-ray radiographs taken over times of 40 – 130 ns. (b) Lineouts of log(intensity) ~ $\Delta OD \sim \rho\kappa\Delta z$, vertically averaged over 120 μm of the 2D x-ray radiographs of driven vanadium (V) Rayleigh-Taylor (RT) samples. Here, ΔOD, ρ, κ, and Δz correspond to modulation in optical depth, density, opacity, and foil thickness for the V sample, respectively. The smooth curves are fitted with single-mode sinusoids with a wavelength of $\lambda = 60$ μm, adjusting only the amplitude.

Fig. 5. Examples of the backlighter spectral characterization and instrument spatial resolution. (a) Radiograph of a vanadium step wedge at the face of the gated MCP. (b) Analysis of the step wedge change in optical depth vs. thickness of the V steps, showing a monochromatic 5.2 keV x-ray source gives a good fit. (c) Radiograph of a backlit Au resolution grid, used to characterize the instrument spatial resolution. (d) The resulting modulation transfer function (MTF) from analysis of the x-ray grid.

Fig. 6. Measured and simulated Rayleigh-Taylor (RT) growth. (a) The RT growth factors (measured ripple amplitude divided by initial amplitude) vs. time. The solid red square plotting symbols give the experimental data. The top curve (dot-dashed orange) gives the result from the 2D simulation with strength set to zero. At t = 70 ns, this no-strength simulation gives growth factor of GF = 67, which is a factor of ~6 higher than the experimental GF. The next highest curve (dotted green) gives the result from using the Steinberg-Guinan (SG) model with nominal (default) input parameters for vanadium. The next highest curve after that (dashed blue) give the results using PTW strength model, with default input parameters for vanadium. The solid blue curve corresponds to the PTW model, with the default vanadium input parameters γ, y_0, s_0 multiplied by 1/800, 0.60, and 0.68. The solid green curve gives the result from using the Steinberg-Guinan model with an overall multplier of 2.3. The lowest curve (solid orange) corresponds to an analytic approach treating the material strength as an effective lattice viscosity, with a constant value of $\mu = 400$ poise. The inset gives peak strength from the simulations that matched the RT experiment, for both the SG and PTW models vs peak pressure for a series of shots where the peak pressure varied from 770 – 950 kbar. The straight line in the inset is a fit to these data. Both models, once fitted to the RT data, give the same predicted peak strength. (b) Measured,

simulated, and analytic RT dispersion curves, given as growth factor vs. perturbation wavelength at a time of 70 ns. The solid black circle plotting symbols correspond to 2D radiation-hydrodynamics simulations with material strength set to zero; the blue diamond solid plotting symbols correspond to a simulation with the PTW strength model adjusted to fit the experiment. The square red plotting symbols at $\lambda = 40$ μm and 60 μm correspond to the experimental measurements. The smooth curves correspond to the analytic viscous RT model assuming viscosities of (from the top) 0, 100, 200, 400, and 800 poise.

Fig. 7. Sample results from the multiscale simulations of this V-RT experiment. [Becker, 2009] Shown are the V-RT ripple from the simulation at t ~ 70 ns. The color scale gives the natural log of the screw dislocation density (top), screw dislocation velocity (middle), and strain rate (bottom). [Becker, 2009]

(a)

[Regazzoni et al, Acta Met. (1987);
M.A. Meyers, text (1994)]

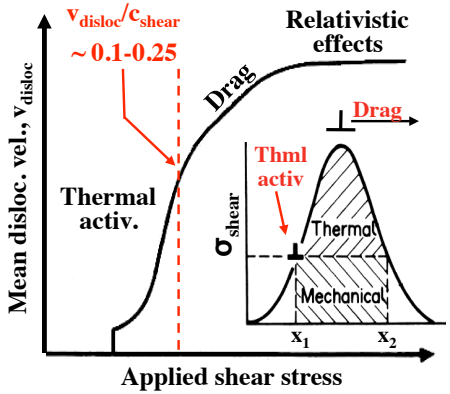

(b)

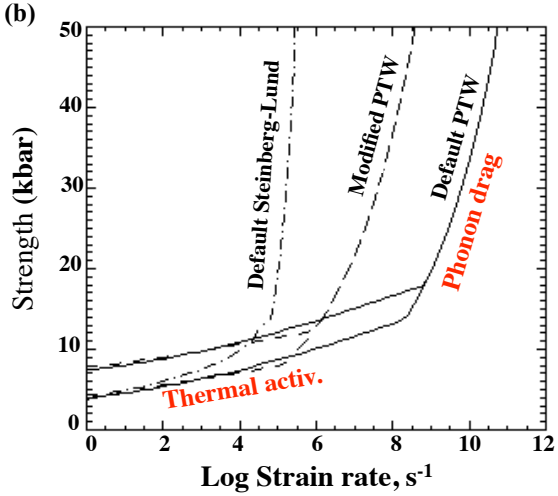

Fig. 1

(a)

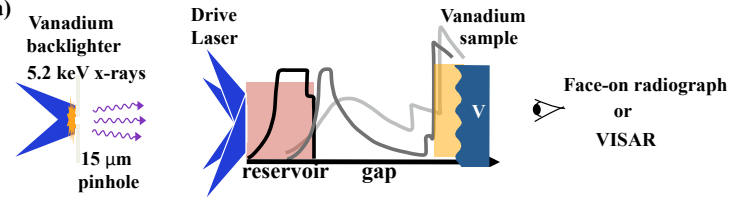

(b)

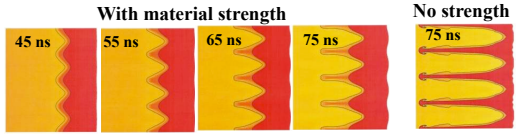

Fig. 2

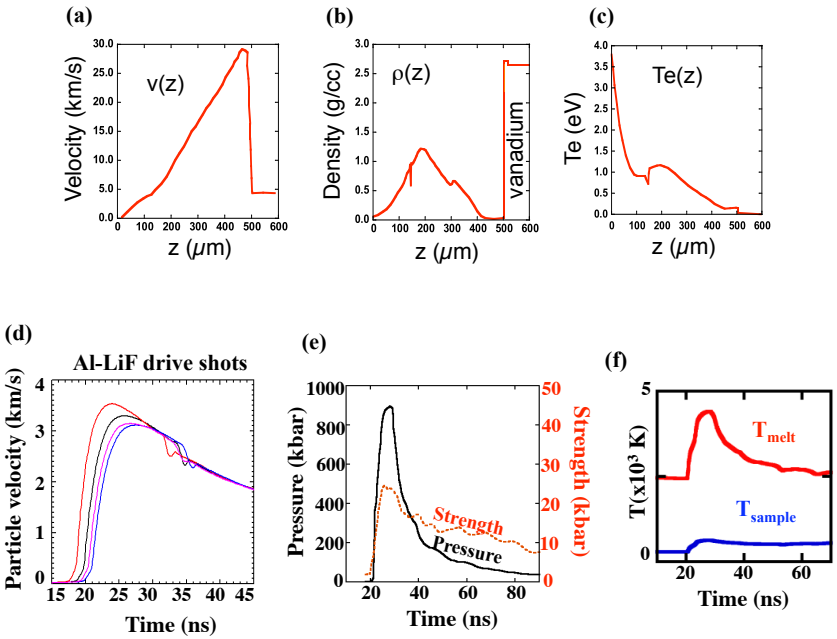
(a)
v(z)
Velocity (km/s)
z (μm)
(b)
ρ(z)
vanadium
Density (g/cc)
z (μm)
(c)
Te(z)
Te (eV)
z (μm)
(d)
Al-LiF drive shots
Particle velocity (km/s)
Time (ns)
(e)
Strength
Pressure
Pressure (kbar)
Strength (kbar)
Time (ns)
(f)
T_melt
T_sample
T(x10^3 K)
Time (ns)

Fig. 3

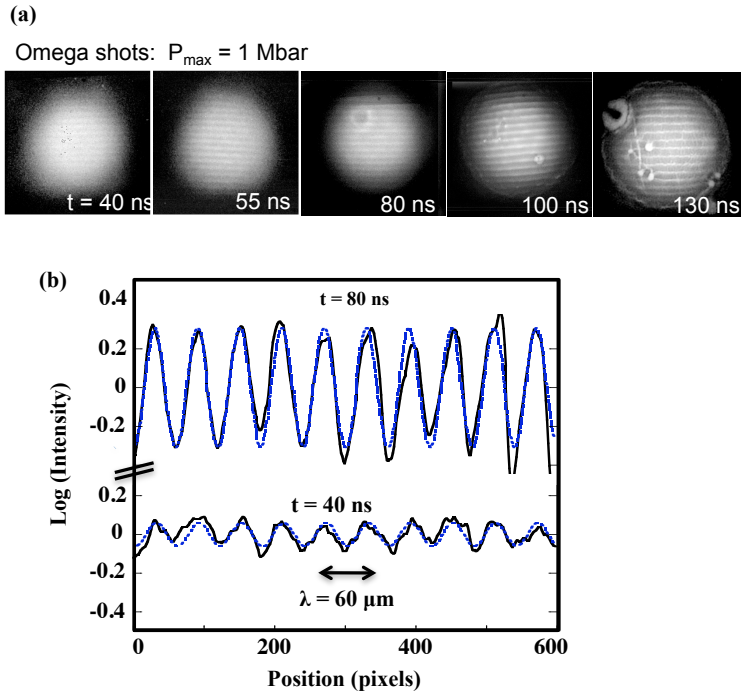
(a)
Omega shots: P_max = 1 Mbar
t = 40 ns
55 ns
80 ns
100 ns
130 ns
(b)
t = 80 ns
t = 40 ns
λ = 60 μm
Log (Intensity)
Position (pixels)

Fig. 4

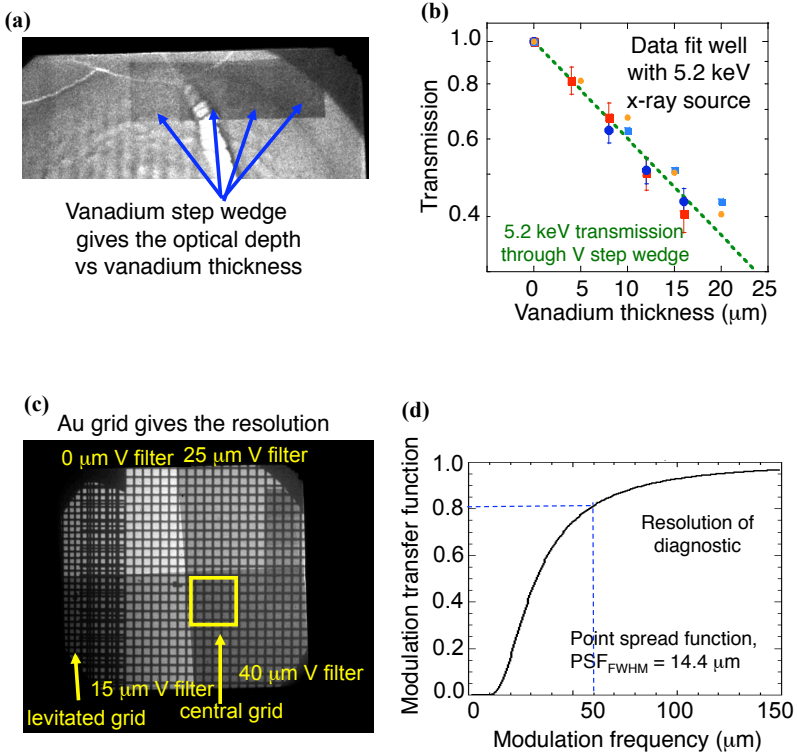
(a)
Vanadium step wedge
gives the optical depth
vs vanadium thickness
(b)
Transmission
Data fit well
with 5.2 keV
x-ray source
5.2 keV transmission
through V step wedge
Vanadium thickness (μm)
(c)
Au grid gives the resolution
0 μm V filter
25 μm V filter
15 μm V filter
40 μm V filter
levitated grid
central grid
(d)
Modulation transfer function
Resolution of
diagnostic
Point spread function,
PSF_FWHM = 14.4 μm
Modulation frequency (μm)

Fig. 5

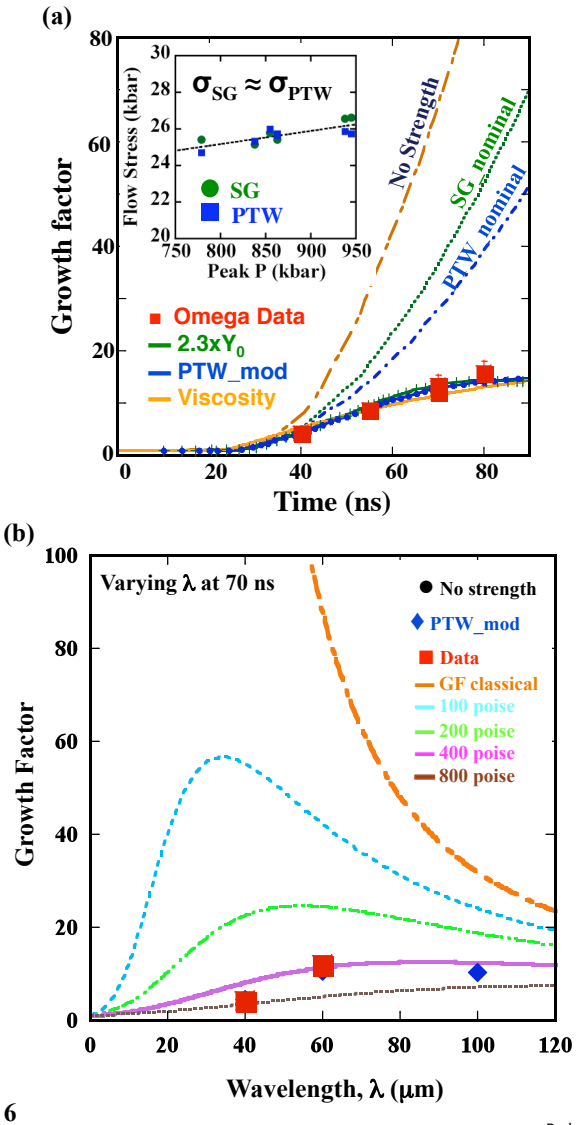
(a)
Growth factor
Time (ns)
Flow Stress (kbar)
Peak P (kbar)
σSG ≈ σPTW
SG
PTW
No Strength
SG nominal
PTW nominal
Omega Data
2.3xY0
PTW_mod
Viscosity
(b)
Varying λ at 70 ns
No strength
PTW_mod
Data
GF classical
100 poise
200 poise
400 poise
800 poise
Growth Factor
Wavelength, λ (μm)

Fig. 6

ALE3D simulation of V-RT evolution using the multiscale strength model, t ~ 70 ns

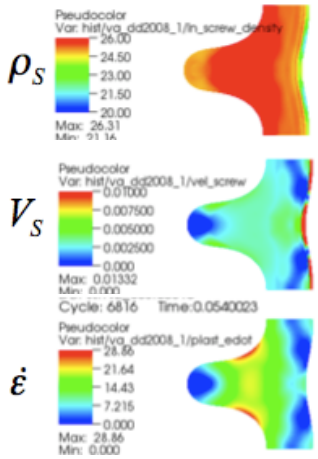

Fig. 7